Inorganic Chemistry
Article
pubs.acs.org/IC

Structural and Magnetic Phase Transitions in the $A_nB_nO_{3n-2}$ Anion-Deficient Perovskites $Pb_2Ba_2BiFe_5O_{13}$ and $Pb_{1.5}Ba_{2.5}Bi_2Fe_6O_{16}$

A. M. Abakumov,*[†,∥] M. Batuk,[†] A. A. Tsirlin,[‡,§] O. A. Tyablikov,[∥] D. V. Sheptyakov,[⊥] D. S. Filimonov,[∥] K. V. Pokholok,[∥] V. S. Zhidal,[∥] M. G. Rozova,[∥] E. V. Antipov,[∥] J. Hadermann,[†] and G. Van Tendeloo[†]

[†]Electron Microscopy for Materials Research (EMAT), University of Antwerp, Groenenborgerlaan 171, B-2020, Antwerp, Belgium
[‡]National Institute of Chemical Physics and Biophysics, 12618 Tallinn, Estonia
[§]Max Planck Institute for Chemical Physics of Solids, Nöthnitzer Strasse 40, 01187 Dresden, Germany
[∥]Department of Chemistry, Moscow State University, 119991 Moscow, Russia
[⊥]Laboratory for Neutron Scattering, Paul Scherrer Institut, CH-5232 Villigen, Switzerland

Supporting Information

ABSTRACT: Novel anion-deficient perovskite-based ferrites $Pb_2Ba_2BiFe_5O_{13}$ and $Pb_{1.5}Ba_{2.5}Bi_2Fe_6O_{16}$ were synthesized by solid-state reaction in air. $Pb_2Ba_2BiFe_5O_{13}$ and $Pb_{1.5}Ba_{2.5}Bi_2Fe_6O_{16}$ belong to the perovskite-based $A_nB_nO_{3n-2}$ homologous series with n = 5 and 6, respectively, with a unit cell related to the perovskite subcell a_p as $a_p\sqrt{2} \times a_p \times na_p\sqrt{2}$. Their structures are derived from the perovskite one by slicing it with $1/2[110]_p(\bar{1}01)_p$ crystallographic shear (CS) planes. The CS operation results in $(\bar{1}01)_p$-shaped perovskite blocks with a thickness of $(n - 2)$ FeO_6 octahedra connected to each other through double chains of edge-sharing FeO_5 distorted tetragonal pyramids which can adopt two distinct mirror-related configurations. Ordering of chains with a different configuration provides an extra level of structure complexity. Above $T \approx 750$ K for $Pb_2Ba_2BiFe_5O_{13}$ and $T \approx 400$ K for $Pb_{1.5}Ba_{2.5}Bi_2Fe_6O_{16}$ the chains have a disordered arrangement. On cooling, a second-order structural phase transition to the ordered state occurs in both compounds. Symmetry changes upon phase transition are analyzed using a combination of superspace crystallography and group theory approach. Correlations between the chain ordering pattern and octahedral tilting in the perovskite blocks are discussed. $Pb_2Ba_2BiFe_5O_{13}$ and $Pb_{1.5}Ba_{2.5}Bi_2Fe_6O_{16}$ undergo a transition into an antiferromagnetically (AFM) ordered state, which is characterized by a G-type AFM ordering of the Fe magnetic moments within the perovskite blocks. The AFM perovskite blocks are stacked along the CS planes producing alternating FM and AFM-aligned Fe−Fe pairs. In spite of the apparent frustration of the magnetic coupling between the perovskite blocks, all n = 4, 5, 6 $A_nFe_nO_{3n-2}$ (A = Pb, Bi, Ba) feature robust antiferromagnetism with similar Néel temperatures of 623−632 K.

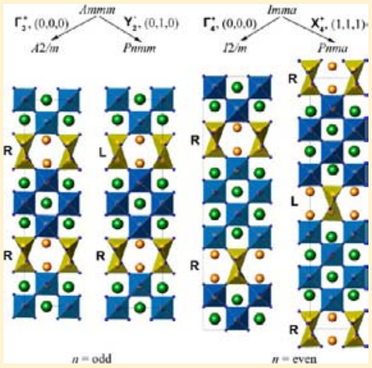

1. INTRODUCTION

The perovskite-based $A_nB_nO_{3n-2}$ homologous series is drastically different from the majority of anion-deficient perovskites.[1] In the $A_nB_nO_{3n-2}$ compounds, the oxygen deficiency is accommodated by a periodic shear operation,[2,3] in contrast to a conventional mechanism that involves ordered or disordered patterns of oxygen vacancies.[4,5] The $A_nB_nO_{3n-2}$ structure can be represented as a stacking of the ABO_2 and O_2 layers along the $[10\bar{1}]_p$ perovskite direction. These layers form quasi-2D perovskite blocks shaped by the $(\bar{1}01)_p$ lattice planes. A single O_2 layer is subtracted at the interface between the two perovskite blocks, and the resulting gap is closed by displacement of one block with respect to the other by a $1/2[110]_p$ lattice vector (see Figure 8 from Abakumov et al.[1]). This crystallographic shear (CS) operation partially eliminates point oxygen vacancies along the interface, transforms pairs of corner-sharing BO_6 octahedra into columns of edge-sharing BO_5 distorted tetragonal pyramids, and creates six-sided tunnels occupied by the lone pair A cations. The homologous series is then formed by varying the thickness of the perovskite blocks between the $1/2[110]_p(\bar{1}01)_p$ CS planes. This thickness (i.e., the number of remaining octahedral units) can be expressed as $n - 2$, where n is the homologue number in the $A_nB_nO_{3n-2}$ formula.

An additional level of structural complexity of the $A_nB_nO_{3n-2}$ perovskites arises from two possible configurations of the tetragonal pyramidal chains. These configurations are related by a mirror operation and arbitrarily called left (L) and right (R) (Figure 1). At room temperature, the n = 4 $Pb_{2-x}Sr_xFe_2O_5$ compounds feature a structure with an ordered arrangement of the L and R chains.[6,7] The $1/2[110]_p(\bar{1}01)_p$ CS planes with either L or R chains alternate in the structure according to the −L−R−L−R− sequence. A similar arrangement of the L and R chains was also observed in the transmission electron microscopy study of the n = 4 $Pb_2Mn_2O_5$ compound.[8] In

Received: December 5, 2012
Published: February 13, 2013

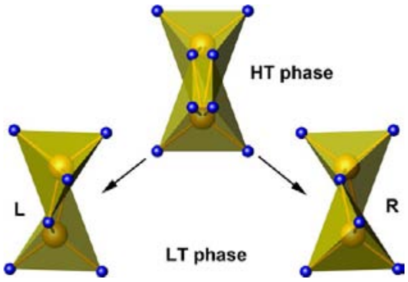

Figure 1. Configurations of the chains of FeO_5 tetragonal pyramids in the $A_nB_nO_{3n-2}$ structures. Left (L) and right (R) configurations are mirror related and occur in an ordered manner in the low-temperature (LT) phases. High-temperature (HT) phase features a disordered arrangement, which is shown as averaged L and R configurations.

$Pb_{2-x}Ba_xFe_2O_5$, the chains are disordered above $T \approx 540$ K (Figure 1) and become ordered at lower temperatures following an order−disorder phase transition.[9] In the crystal structure of the homologues with higher numbers, $n = 5$ $Pb_{2.9}Ba_{2.1}Fe_4TiO_{13}$ and $Pb_{2.85}Ba_{2.15}Fe_4SnO_{13}$ and $n = 6$ $Pb_{3.8}Bi_{0.2}Ba_2Fe_{4.2}Ti_{1.8}O_{16}$, neutron powder diffraction detected the disordered chains at $T \approx 550$ K.[1,10] Therefore, one can expect structural phase transitions related to the chain ordering in these structures. However, their low-temperature structures have not been determined yet.

The increasing oxygen content with increasing n in the $A_nB_nO_{3n-2}$ homologous series requires charge compensation by heterovalent replacements in the A and/or B sublattices. Instead of mixing cations in the B sublattice ($Fe^{3+} \rightarrow Ti^{4+}$, Sn^{4+}), we employed a different synthesis strategy based on the heterovalent $Pb^{2+} \rightarrow Bi^{3+}$ replacement in the A sublattice. This way, the novel $n = 5$ and 6 $A_nFe_nO_{3n-2}$ (A = Pb, Ba, Bi) ferrites have been prepared. We monitored their phase transitions between the disordered high-temperature (HT) and the ordered low-temperature (LT) polymorphs. Using the LT crystal structure, we were also able to determine the spin arrangement in these antiferromagnetically ordered materials. We therefore report on the synthesis, LT and HT crystal structure, magnetic structures, and magnetic properties of the $A_nFe_nO_{3n-2}$ (A = Pb, Ba, Bi) perovskite-based ferrites with $n = 5$, 6.

2. EXPERIMENTAL SECTION

$Pb_2Ba_2BiFe_5O_{13}$ and $Pb_{2-x}Ba_{2+x}Bi_2Fe_6O_{16}$ ($x = 0$−1, $\Delta x = 0.2$) samples were prepared by a solid-state reaction of PbO, $BaCO_3$, Bi_2O_3, and Fe_2O_3. The initial components were mixed in stoichiometric amounts, ground thoroughly, and pressed into pellets. Thermal treatment included annealing at 750 °C for 25 h and at 800 °C for 25 h in air with intermediate regrinding.

The phase composition of the samples was analyzed using X-ray powder diffraction (XRPD) performed with a Huber G670 Guinier diffractometer (Cu $K\alpha_1$ radiation, curved Ge(111) monochromator, transmission mode, image plate). The cation composition has been measured by energy-dispersive X-ray (EDX) analysis in a Jeol JEM5510 scanning electron microscope equipped with an INCA EDX system (Oxford instruments). Measured cation concentrations agree with the nominal chemical composition within experimental error ($Pb_2Ba_2BiFe_5O_{13}$ (atom. %): exp 8.7(4):9.1(4):4.5(3):21.3(8), calcd 8.7:8.7:4.35:21.7. $Pb_{1.5}Ba_{2.5}Bi_2Fe_6O_{16}$ (atom. %): exp 5.0(4):9.3(4):7.5(4):21.4(10); calcd 5.35:8.9:7.1:21.4).

High-resolution synchrotron X-ray powder diffraction (SXPD) data were collected at the ID31 beamline of the European Synchrotron Radiation Facility (ESRF, Grenoble, France) using a wavelength of ∼0.4 Å and eight scintillation detectors, each preceded by a Si (111) analyzer crystal. The powder sample was contained in a thin-walled quartz capillary that was spun during the experiment. The temperature of the sample was controlled by a He-flow cryostat (temperature range 10−300 K) and hot-air blower (300−1000 K).

Neutron powder diffraction (NPD) data were collected with the high-resolution powder diffractometer HRPT (Paul Scherrer Institut (PSI), Switzerland) at a wavelength of 1.8857 Å with the use of a standard orange cryostat and radiation-type furnace to cover the temperature range from 1.5 to 1000 K.

Rietveld refinement of the crystal and magnetic structure against the powder diffraction data was performed with the JANA2006 package.[11]

Transmission electron microscopy (TEM) was performed with a FEI Tecnai G2 microscope operated at 200 kV. TEM specimens were prepared by grinding the sample in ethanol and depositing the dispersion on a copper grid covered with a holey carbon film. Sample was analyzed by means of selected area electron diffraction (ED) at different temperatures and high-resolution high-angle annular dark field scanning transmission electron microscopy (HAADF-STEM). Simulated HAADF-STEM images were calculated using the QSTEM 2.0 software.[12]

Magnetic susceptibility was measured with a Quantum Design MPMS SQUID magnetometer and vibrating sample magnetometer (VSM) installed in the Quantum Design PPMS. Measurements were performed in the 2−900 K temperature range and applied fields up to 5 T. Data above 380 K were collected using the oven setup that operates in high vacuum (10^{-5} mbar).

3. RESULTS

3.1. High-Temperature (HT) and Low-Temperature (LT) Structures. XRPD revealed formation of a single-phase $Pb_2Ba_2BiFe_5O_{13}$ compound and $Pb_{2-x}Ba_{2+x}Bi_2Fe_6O_{16}$ solid solutions with the $0 < x \leq 0.7$ homogeneity range (see Table S1, Supporting Information, for compositional dependence of the lattice parameters). As the $x = 0$ sample was obtained with a small amount of admixture, the single-phase $Pb_{1.5}Ba_{2.5}Bi_2Fe_6O_{16}$ ($x = 0.5$) composition was selected for further investigation. Unit cell metrics correspond to $a_p\sqrt{2} \times a_p \times 5a_p\sqrt{2}$ and $a_p\sqrt{2} \times a_p \times 6a_p\sqrt{2}$ for $Pb_2Ba_2BiFe_5O_{13}$ and

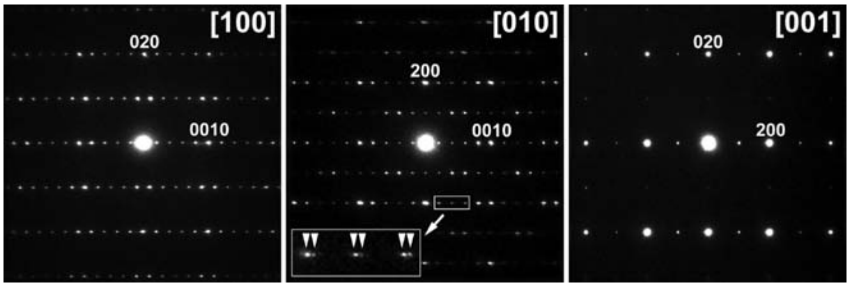

Figure 2. Electron diffraction patterns of $Pb_2Ba_2BiFe_5O_{13}$. Insert in the [010] ED pattern shows reflection splitting due to monoclinic distortion and twinning.

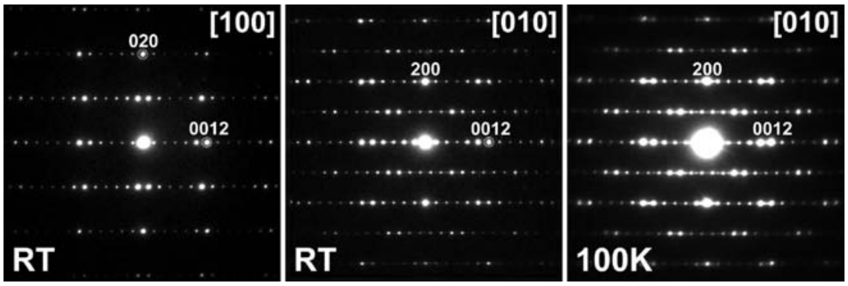

Figure 3. Electron diffraction patterns of $Pb_{1.5}Ba_{2.5}Bi_2Fe_6O_{16}$.

$Pb_{1.5}Ba_{2.5}Bi_2Fe_6O_{16}$, respectively, which is characteristic of the $n = 5$ and 6 members of the $A_nB_nO_{3n-2}$ homologous series.

Room-temperature ED patterns of $Pb_2Ba_2BiFe_5O_{13}$ (Figure 2) confirm the lattice parameters and show the hkl: $k + l = 2n$ reflection condition due to the A-centered lattice. Very weak reflections with k = odd in the [001] ED pattern are attributed to first-order Laue zone reflections, according to their intensity variation with respect to the scattering angle. Reflections in the [010] ED pattern are split: the splitting direction is parallel to the $00l$ reciprocal lattice row, and the splitting magnitude increases with increasing distance from the $00l$ row. This indicates a monoclinic distortion with $\beta \neq 90°$ and twinning with the (001) twin plane. The monoclinic distortion is supported by a pronounced reflection splitting observed in the SXPD patterns (see reflections 1 1 5, 2 1 3, and 2 0 10 in Figure S1, Supporting Information). The reflection splitting gradually decreases upon heating and eventually disappears around T = 750 K, indicating a phase transition from the low-temperature (LT) monoclinic phase to the high-temperature (HT) orthorhombic phase. A slight residual broadening remains visible, however, on SXPD patterns up to T = 1150 K.

Room-temperature ED patterns of $Pb_{1.5}Ba_{2.5}Bi_2Fe_6O_{16}$ show the hkl: $h + k + l = 2n$ reflection condition, which is characteristic of a body-centered unit cell (Figure 3). However, in the [010] ED pattern diffuse streaks parallel to the **c*** axis are visible. These streaks show an intensity modulation centered at the $h0l$: $h + l \neq 2n$ positions. The streaks can be attributed to local ordering, thus violating the I-centered lattice. On cooling, these streaks are concentrated into $h0l$: $h + l \neq 2n$ reflections (Figure 3), indicating a continuous transformation from the HT I-centered orthorhombic structure to the LT structure with a primitive unit cell. On heating, the diffuse streaks loose the intensity modulation above 400 K and vanish completely above 600 K (Figure S2, Supporting Information). In contrast to $Pb_2Ba_2BiFe_5O_{13}$, the temperature evolution of the SXPD patterns does not reveal a pronounced reflection splitting (Figure S1, Supporting Information), except some broadening of the reflections with $h, l \neq 0$, which can be attributed to planar defects arising in the LT phase below the transition temperature (see Discussion for details). The superlattice reflections violating the I-centering are too weak to be observed even on the SXPD patterns, but they can be clearly seen on the neutron powder diffraction data.

The transformation from the HT phase to the LT phase was monitored with NPD in the temperature range of 1.5−1150 K for $Pb_2Ba_2BiFe_5O_{13}$ and 1.5−950 K for $Pb_{1.5}Ba_{2.5}Bi_2Fe_6O_{16}$. In both cases, the temperature dependence of the unit cell volume does not demonstrate any discontinuity that is typical for a second-order phase transition (Figure S3, Supporting Information). The monoclinic angle β for $Pb_2Ba_2BiFe_5O_{13}$ deviates from 90° with an onset at ~750 K, in agreement with the SXPD observations. On the NPD patterns of $Pb_{1.5}Ba_{2.5}Bi_2Fe_6O_{16}$, weak and diffuse $h0l$: $h + l \neq 2n$ reflections become visible at ~400 K, which is taken as the temperature of the phase transition.

Analysis of reflection conditions on the ED, SXPD, and NPD patterns allowed us to propose $Ammm$ and $Imma$ as the most symmetric space groups for the HT $Pb_2Ba_2BiFe_5O_{13}$ and $Pb_{1.5}Ba_{2.5}Bi_2Fe_6O_{16}$ structures, respectively. For the LT structures, the isotropy subgroups $A2/m$ and $Pnma$ were selected according to the observations performed with all three diffraction techniques. The initial atomic coordinates for refinement from NPD data were obtained from the $Pb_{2.9}Ba_{2.1}Fe_4TiO_{13}$ and $Pb_{3.8}Bi_{0.2}Ba_2Fe_{4.2}Ti_{1.8}O_{16}$ structures.[1] In $Pb_2Ba_2BiFe_5O_{13}$ all Pb atoms were found in the six-sided tunnels at the CS planes between the perovskite blocks. In the $Pb_{1.5}Ba_{2.5}Bi_2Fe_6O_{16}$ structure, there is not enough Pb to occupy completely the position in the six-sided tunnels. A mixed occupation of this position by Pb and Bi was assumed, because the oxygen coordination of this position is unsuited for the large Ba^{2+} cations. As no clear indication of the ordering of Ba and Bi was observed, these cations were randomly distributed over the A sites of the perovskite blocks. Both structures feature the splitting of the O4 position, which forms a common edge of the tetragonal FeO_5 pyramids at the interface between the perovskite blocks (Figure 1). This position was refined with an occupancy factor of 1/2.

Atomic coordinates of the LT phases were obtained by a transformation of the HT structures into the corresponding isotropy subgroups. The O4 atom then splits into two closely placed positions. Only one position was left in the refinement with full occupancy. The magnetic contribution was taken into account when necessary (see below). For the LT structures, the common atomic displacement parameters (ADPs) were refined for the A and B cations and oxygens. Crystallographic data for the LT and HT $Pb_2Ba_2BiFe_5O_{13}$ and $Pb_{1.5}Ba_{2.5}Bi_2Fe_6O_{16}$ structures are provided in Table 1; atomic parameters and interatomic distances of the LT and HT phases are listed in Tables 2−5 and 6−9, respectively. Experimental, calculated, and difference NPD profiles are shown in Figure 4.

LT crystal structures of $Pb_2Ba_2BiFe_5O_{13}$ and $Pb_{1.5}Ba_{2.5}Bi_2Fe_6O_{16}$ are shown in Figure 5. The perovskite blocks in these $n = 5$ and 6 structures have a thickness of three and four FeO_6 octahedra, respectively. Blocks are connected along the c axis through the chains of the edge-sharing distorted tetragonal FeO_5 pyramids. Pyramidal chains are linked by common corners to the octahedra of the perovskite blocks and delimit the six-sided tunnels that are filled with double columns of the lone-pair cations (preferentially Pb^{2+}). Bond valence sums calculated for the Fe atoms agree well with the formal oxidation state of +3 for the Fe cations (Tables 4 and 5), as calculated from the chemical compositions and confirmed by

Table 1. Selected Parameters of the Rietveld Refinements of the $Pb_2Ba_2BiFe_5O_{13}$ and $Pb_{1.5}Ba_{2.5}Bi_2Fe_6O_{16}$ Structures from NPD Data

	$Pb_2Ba_2BiFe_5O_{13}$		$Pb_{1.5}Ba_{2.5}Bi_2Fe_6O_{16}$	
T, K	300	1000	300	950
space group	*A*2/*m*	*Ammm*	*Pnma*	*Imma*
a, Å	5.7530(2)	5.8145(1)	5.7453(2)	5.8042(1)
b, Å	3.96018(9)	4.00876(7)	3.9492(1)	3.99156(9)
c, Å	27.018(1)	27.2477(6)	32.851(1)	33.1437(9)
β, deg	90.777(4)			
Z	2	2	2	2
cell volume, $Å^3$	615.49(4)	635.12(3)	745.36(7)	767.88(5)
calcd density, g/cm^3	7.472	7.241	7.408	7.191
radiation	neutrons, $\lambda = 1.8857$ Å	neutrons, $\lambda = 1.8857$ Å	neutrons, $\lambda = 1.8857$ Å	neutrons, $\lambda = 1.8857$ Å
R_F, R_P, R_{wP}	0.018, 0.046, 0.059	0.031, 0.045, 0.056	0.021, 0.038, 0.051	0.038, 0.032, 0.042

Table 2. Atomic Parameters of the LT ($T = 300$ K) $Pb_2Ba_2BiFe_5O_{13}$ Structure

atom	position	*x*/*a*	*y*/*b*	*z*/*c*	U_{iso}, $Å^2$
Pb1	4*i*	0.492(1)	1/2	0.3076(2)	0.0175(9)
Ba1[a]	4*i*	−0.002(1)	0	0.0956(2)	0.0175(9)
Ba2[a]	2*d*	1/2	1/2	1/2	0.0175(9)
Fe1	4*i*	−0.014(1)	0	0.2924(2)	0.0063(4)
Fe2	4*i*	0.490(1)	0	0.3984(2)	0.0063(4)
Fe3	2*b*	0	0	1/2	0.0063(4)
O1	4*i*	0.499(2)	1/2	0.3883(3)	0.0101(4)
$O2_1$	4*i*	0.241(2)	0	0.4457(5)	0.0101(4)
$O2_2$	4*i*	0.247(2)	0	0.5537(6)	0.0101(4)
$O3_1$	4*i*	0.245(2)	0	0.3352(3)	0.0101(4)
$O3_2$	4*i*	0.278(1)	0	0.6665(3)	0.0101(4)
O4	4*i*	0.053(1)	0	0.2206(3)	0.0101(4)
O5	2*a*	0	0	0	0.0101(4)

[a] Occupancy 2/3Ba + 1/3 Bi.

Table 3. Atomic Parameters of the LT ($T = 300$ K) $Pb_{1.5}Ba_{2.5}Bi_2Fe_6O_{16}$ Structure

atom	position	*x*/*a*	*y*/*b*	*z*/*c*	U_{iso}, $Å^2$
Pb1[a]	4*c*	0.988(2)	3/4	0.4538(2)	0.028(1)
Ba1[b]	4*c*	0.486(2)	3/4	0.3663(3)	0.028(1)
Ba2[b]	4*c*	0.494(3)	3/4	0.2079(3)	0.028(1)
Fe1	4*c*	0.494(2)	1/4	0.4657(2)	0.0113(4)
Fe2	4*c*	0.484(1)	1/4	0.1234(2)	0.0113(4)
Fe3	4*c*	0.514(1)	3/4	0.7073(2)	0.0113(4)
O1	4*c*	0.498(3)	3/4	0.1143(3)	0.0162(4)
$O2_1$	4*c*	0.761(2)	3/4	0.6609(4)	0.0162(4)
$O2_2$	4*c*	0.221(2)	1/4	0.1577(4)	0.0162(4)
$O3_1$	4*c*	0.230(2)	1/4	0.4303(4)	0.0162(4)
$O3_2$	4*c*	0.748(2)	3/4	0.9284(4)	0.0162(4)
O4	4*c*	0.445(1)	3/4	0.4775(3)	0.0162(4)
O5	4*c*	0.513(2)	1/4	0.7034(4)	0.0162(4)
O6	4*c*	0.742(2)	3/4	0.7535(4)	0.0162(4)

[a] Occupancy 3/4Pb + 1/4 Bi. [b] Occupancy 5/8Ba + 3/8 Bi.

Mössbauer spectroscopy. The common feature of both structures is displacement of the Fe2 atoms along the *c* axis from the center of the $Fe2O_6$ octahedron toward the center of the perovskite block. This displacement results in two short (1.89−1.98 Å) and two long (2.16−2.26 Å) equatorial Fe−O distances. The coordination environment of the A cations in the six-sided tunnels features one short A−O distance of 2.18−2.24 Å, which is characteristic of a covalent bonding between the oxygen atom and the lone-pair A cation.[13,14]

The refined crystal structures of $Pb_2Ba_2BiFe_5O_{13}$ and $Pb_{1.5}Ba_{2.5}Bi_2Fe_6O_{16}$ have been confirmed by HAADF-STEM imaging (Figure 6). The contrast on these images is roughly proportional to the difference in the scattering power at the atomic columns, so that the images can be considered—with some simplification—as a map of the projected scattering density of the crystal. The brighter dots in the [100] and [010] HAADF-STEM images correspond to the projections of the heavier atomic columns (Pb, Bi, and Ba). The theoretical images calculated with the refined LT structures are in good agreement with the experimental ones, thus confirming the correctness of the structure solution. Stacking faults leading to perovskite lamellas with different thicknesses, which are very common in perovskite-based homologous series, are only occasionally found (Figure S4, Supporting Information).

3.2. Magnetic Structures of $Pb_2Ba_2BiFe_5O_{13}$ and $Pb_{1.5}Ba_{2.5}Bi_2Fe_6O_{16}$.

Below $T \approx 650$ K, magnetic reflections develop on the NPD patterns of both $Pb_2Ba_2BiFe_5O_{13}$ and $Pb_{1.5}Ba_{2.5}Bi_2Fe_6O_{16}$ compounds. The magnetic origin of these reflections is confirmed by their absence in the SXPD patterns. The magnetic reflections can be indexed with $\mathbf{k} = (1, 1/2, 1/2)$ and $(0, 1/2, 1/2)$ propagation vectors for $Pb_2Ba_2BiFe_5O_{13}$ and $Pb_{1.5}Ba_{2.5}Bi_2Fe_6O_{16}$, respectively, indicating an antiferomagnetic (AFM) ordering. Symmetry analysis of the magnetic structures has been performed with the ISODISTORT software.[15] Since the crystallographic transition temperature for $Pb_2Ba_2BiFe_5O_{13}$ is higher than the Néel temperature, the *A*2/*m* space group of the LT phase was used in symmetry analysis. The $P_S\bar{1}$ magnetic space group provides the correct description of the magnetic structure. For the $Pb_{1.5}Ba_{2.5}Bi_2Fe_6O_{16}$ phase, the P_b2_1/c and B_b2/b magnetic space groups were selected for the LT and HT structures, respectively. The symmetry operators of the magnetic groups, atomic coordinates of the magnetic atoms, and magnetic moment components are provided in Tables S2−S7, Supporting Information.

All structures under investigation feature three independent magnetic iron atoms per unit cell. However, refinement revealed that their magnetic moments are identical within the standard deviations. Therefore, the components of the magnetic moments on the Fe1, Fe2, and Fe3 atoms were restricted to produce the same total value of the magnetic moment. The ordered magnetic moments at $T = 1.5$ K were refined to be 3.85(2) μ_B and 3.90(2) μ_B for $Pb_2Ba_2BiFe_5O_{13}$ and $Pb_{1.5}Ba_{2.5}Bi_2Fe_6O_{16}$, respectively. Using the temperature dependence of the ordered magnetic moment (Figure S5, Supporting Information), we estimated the Néel temperatures of $T_N = 623(6)$ K for $Pb_2Ba_2BiFe_5O_{13}$ and $T_N = 632(4)$ K for $Pb_{1.5}Ba_{2.5}Bi_2Fe_6O_{16}$.

Magnetic structures of $Pb_2Ba_2BiFe_5O_{13}$ and $Pb_{1.5}Ba_{2.5}Bi_2Fe_6O_{16}$ are shown in Figure 7. In terms of the crystallographic unit cell, the magnetic moments in both structures are strictly aligned along the *b* axis. The perovskite blocks feature G-type AFM ordering with antiparallel magnetic moments on all nearest neighbors. AFM perovskite blocks are stacked along the chains of the FeO_5 tetragonal pyramids in such a way that parallel and aniparallel spins alternate along the zigzag pathway between the Fe atoms in the chain.

Table 4. Selected Interatomic Distances for the LT (T = 300 K) $Pb_2Ba_2BiFe_5O_{13}$ Structure

Pb1–O1	2.18(1) × 1	Ba2–O1	3.019(8) × 2	Fe2–O1	2.000(2) × 2
Pb1–O3$_1$	2.557(7) × 2	Ba2–O2$_1$	2.87(1) × 4	Fe2–O2$_1$	1.93(2) × 1
Pb1–O3$_2$	2.475(6) × 2	Ba2–O2$_2$	2.86(1) × 4	Fe2–O2$_2$	1.98(2) × 1
Pb1–O4	2.734(9) × 1	Ba2–O5	2.8767(2) × 2	Fe2–O3$_2$	2.22(1) × 1
				BVS(Fe2)	2.81
Ba1–O1	2.90(1) × 1	Fe1–O3$_1$	1.87(1) × 1		
Ba1–O1	2.92(1) × 1	Fe1–O3$_2$	1.90(1) × 1	Fe3–O2$_1$	2.03(1) × 2
Ba1–O2$_1$	2.65(1) × 2	Fe1–O4	1.98(1) × 1	Fe3–O2$_2$	2.02(1) × 2
Ba1–O2$_2$	2.70(1) × 2	Fe1–O4	2.023(2) × 2	Fe3–O5	1.9801(1) × 2
Ba1–O3$_1$	3.072(8) × 2	BVS(Fe1)	2.95	BVS(Fe3)	3.05
Ba1–O3$_2$	3.177(8) × 2				
Ba1–O5	2.584(5) × 1				

Table 5. Selected Interatomic Distances for the LT (T = 300 K) $Pb_{1.5}Ba_{2.5}Bi_2Fe_6O_{16}$ Structure

Pb1–O1	2.24(1) × 1	Ba2–O1	3.08(2) × 2	Fe2–O1	1.999(2) × 2
Pb1–O3$_1$	2.54(1) × 2	Ba2–O2$_1$	2.88(1) × 2	Fe2–O2$_1$	1.91(1) × 1
Pb1–O3$_2$	2.54(1) × 2	Ba2–O2$_2$	3.01(2) × 4	Fe2–O2$_2$	1.89(1) × 1
Pb1–O4	2.74(1) × 1	Ba2–O5	2.84(2) × 1	Fe2–O3$_1$	2.26(1) × 1
		Ba2–O5	2.91(2) × 2	Fe2–O3$_2$	2.16(1) × 1
Ba1–O1	2.88(2) × 1	Ba2–O6	2.91(2) × 2	BVS(Fe2)	3.01
Ba1–O1	3.01(2) × 1	Ba2–O6	2.71(1) × 2		
Ba1–O2$_1$	2.59(1) × 2			Fe3–O2$_1$	2.08(1) × 1
Ba1–O2$_2$	2.52(1) × 2	Fe1–O3$_1$	1.91(2) × 1	Fe3–O2$_2$	2.12(1) × 1
Ba1–O3$_1$	3.24(1) × 2	Fe1–O3$_2$	1.92(2) × 1	Fe3–O5	1.9787(8) × 2
Ba1–O3$_2$	3.22(1) × 2	Fe1–O4	1.90(1) × 1	Fe3–O6	2.01(1) × 1
Ba1–O5	2.29(1) × 1	Fe1–O4	2.032(3) × 2	Fe3–O6	2.03(1) × 1
		BVS(Fe1)	2.98	BVS(Fe3)	2.89

Table 6. Atomic Parameters of the HT (T = 1000 K) $Pb_2Ba_2BiFe_5O_{13}$ Structure

atom	position	x/a	y/b	z/c	U_{iso}, Å^2
Pb1	4*j*	1/2	1/2	0.3067(2)	0.045(2)
Ba1[a]	4*i*	0	0	0.0966(3)	0.035(2)
Ba2[a]	2*d*	1/2	1/2	1/2	0.044(4)
Fe1	4*i*	0	0	0.2929(2)	0.018(1)
Fe2	4*j*	1/2	0	0.3977(2)	0.021(1)
Fe3	2*b*	0	0	1/2	0.025(2)
O1	4*j*	1/2	1/2	0.3870(4)	0.036(3)
O2	8*n*	0.249(2)	0	0.4457(3)	0.033(1)
O3	8*n*	0.2667(9)	0	0.3342(2)	0.032(1)
O4[b]	8*n*	0.047(1)	0	0.2185(3)	0.015(2)
O5	2*a*	0	0	0	0.022(3)

[a] Occupancy 2/3Ba + 1/3 Bi. [b] Occupancy 0.5O.

Table 7. Atomic Parameters of the HT (T = 950 K) $Pb_{1.5}Ba_{2.5}Bi_2Fe_6O_{16}$ Structure

atom	position	x/a	y/b	z/c	U_{iso}, Å^2
Pb1[a]	4*e*	0	3/4	0.4531(2)	0.048(2)
Ba1[b]	4*e*	1/2	3/4	0.3680(2)	0.039(2)
Ba2[b]	4*e*	1/2	3/4	0.2064(3)	0.047(1)
Fe1	4*e*	1/2	1/4	0.4647(1)	0.030(1)
Fe2	4*e*	1/2	1/4	0.1223(1)	0.021(1)
Fe3	4*e*	1/2	3/4	0.7092(2)	0.023(2)
O1	4*e*	1/2	3/4	0.1115(2)	0.019(2)
O2	8*i*	0.738(1)	3/4	0.6588(2)	0.038(1)
O3	8*i*	0.2417(9)	1/4	0.4295(2)	0.041(1)
O4[c]	8*i*	0.443(1)	3/4	0.4735(2)	0.027(2)
O5	4*e*	1/2	1/4	0.7054(3)	0.028(1)
O6	4*c*	3/4	3/4	3/4	0.032(2)

[a] Occupancy 3/4Pb + 1/4 Bi. [b] Occupancy 5/8Ba + 3/8 Bi. [c] Occupancy 0.5O.

3.3. $Pb_2Ba_2BiFe_5O_{13}$: Mössbauer Spectroscopy. Mössbauer spectra of $Pb_2Ba_2BiFe_5O_{13}$ were measured in the 78–700 K temperature range. The spectrum measured in the paramagnetic region is shown in Figure 8a. It was fitted with two overlapping doublets, which are designated as A1 and B1. All Fe atoms are in the Fe^{3+} state, according to the isomer shifts (ISs) with respect to the second-order Doppler shift. Taking into account the hyperfine parameters of the doublets (the IS and electric quadrupole splitting ΔE_Q) in combination with the data for other $A_nB_nO_{3n-2}$ homologues,[1,9,10] the "A" doublets were ascribed to the octahedral crystallographic positions while the "B" doublets correspond to the 5-fold-coordinated Fe atoms. The observed ratio of the doublet contributions is about 3:2, in good agreement with the crystallographic data (Table S8, Supporting Information).

Below T_N, the Mössbauer spectra of $Pb_2Ba_2BiFe_5O_{13}$ are magnetically split. The magnetic transition spreads over a broad temperature range, where the magnetic and paramagnetic components coexist. The Mössbauer spectrum measured at 78 K is shown in Figure 8b. All lines in the spectrum are notably broadened presumably because of development of nonuniform local distortions of oxygen polyhedra during the HT–LT phase transition. Accordingly, the spectrum was fitted with two overlapping broadened subspectra. Each of the subspectra consists of a minimum of three overlapped broadened Zeeman sextets, which are slightly different in their hyperfine parameters. This already complex model provides reasonable, although not ideal, fit to the spectrum. Subspectrum "A" with higher values of the ISs and hyperfine magnetic fields (H_{HF}s)

Table 8. Selected Interatomic Distances for the HT (T = 1000 K) $Pb_2Ba_2BiFe_5O_{13}$ Structure

Pb1–O1	2.141(9) × 1	Ba2–O1	3.08(1) × 2	Fe2–O1	2.025(2) × 2
Pb1–O3	2.559(4) × 4	Ba2–O2	2.887(6) × 8	Fe2–O2	1.96(1) × 2
Pb1–O4	2.662(6) × 2	Ba2–O5	2.9073(1) × 2	Fe2–O3	2.199(7) × 2
Ba1–O1	2.941(2) × 2	Fe1–O3	1.916(6) × 2	Fe3–O2	2.069(9) × 4
Ba1–O2	2.728(7) × 4	Fe1–O4	2.045(9) × 1	Fe3–O5	2.0044(1) × 2
Ba1–O3	3.160(6) × 4	Fe1–O4	2.047(2) × 2		
Ba1–O5	2.631(8) × 1				

Table 9. Selected Interatomic Distances for the HT (T = 950 K) $Pb_{1.5}Ba_{2.5}Bi_2Fe_6O_{16}$ Structure

Pb1–O1	2.141(9) × 1	Ba2–O1	3.15(1) × 1	Fe2–O1	2.028(1) × 2
Pb1–O3	2.565(4) × 4	Ba2–O2	2.967(7) × 4	Fe2–O2	1.948(6) × 2
Pb1–O4	2.659(6) × 2	Ba2–O5	2.9023(3) × 2	Fe2–O3	2.221(5) × 2
		Ba2–O5	2.92(1) × 1		
Ba1–O1	2.981(2) × 2	Ba2–O6	2.860(5) × 4	Fe3–O2	2.164(8) × 2
Ba1–O2	2.582(4) × 4			Fe3–O5	1.9998(8) × 2
Ba1–O3	3.220(5) × 4	Fe1–O3	1.895(6) × 2	Fe3–O6	1.983(5) × 2
Ba1–O5	2.43(1) × 1	Fe1–O4	2.075(9) × 1		
		Fe1–O4	2.044(2) × 2		

features negative apparent quadrupole shifts (QSs) and corresponds to the octahedral positions of the Fe^{3+} cations. With lower values of the ISs and H_{HF}s and positive QSs, subspectrum "B" is the signal of 5-fold-coordinated Fe^{3+} (Table S16, Supporting Information). Similar to the paramagnetic data, the ratio between the contributions from the "A" and "B" subsets is close to 3:2.

Thus, the Mössbauer spectra fully corroborate the conclusions inferred from structural analysis and neutron diffraction data: all Fe atoms are in the oxidation state Fe^{3+} and their local environment follows the 3:2 ratio for the 6- and 5-fold oxygen coordination, respectively.

3.4. Magnetic Susceptibility. The magnetic susceptibility of $Pb_2Ba_2BiFe_5O_{13}$ increases with temperature, as typical for an antiferromagnet below the Néel temperature T_N (Figure 9). A very weak upturn observed below 20 K is likely related to the Curie-like paramagnetic contribution of impurities. The linear magnetization curve (inset of Figure 9) together with the field-independent susceptibility excludes any net magnetic moment and rules out possible spin canting in the antiferromagnetically ordered state. Unfortunately, we were unable to track the magnetic susceptibility above T_N because the sample started to decompose in the high-vacuum environment of the oven chamber. Above 600 K, the heating/cooling measurements became irreversible, while the overall increase in the magnetic moment suggested formation of a ferromagnetic impurity. Indeed, scans up to 900 K revealed a well-defined ferromagnetic transition around 860 K that corresponds to the Curie temperature of Fe_3O_4 formed upon reduction of Fe^{3+} in high dynamic vacuum.[17]

In contrast to $Pb_2Ba_2BiFe_5O_{13}$, susceptibility measurements on $Pb_{1.5}Ba_{2.5}Bi_2Fe_6O_{16}$ showed a weak net moment of about 0.04 μ_B/f.u. even in the pristine sample (Figure S6, Supporting Information). This net moment is likely extrinsic because it persists well above $T_N \approx 630$ K. The ferromagnetic signal dwindles only above 730 K (Figure S7, Supporting Information), which is close to the Curie temperature of $BaFe_{12}O_{19}$ and other similar "hexaferrites".[18] The small net moment corresponds to less than 0.1 wt % of the hexaferrite impurity, which is hardly detectable by XRPD and NPD.

Altogether, both $Pb_2Ba_2BiFe_5O_{13}$ and $Pb_{1.5}Ba_{2.5}Bi_2Fe_6O_{16}$ are antiferromagnets without any appreciable signature of spin canting or additional magnetic transitions below T_N.

4. DISCUSSION

The $A_nB_nO_{3n-2}$ structure and space symmetry of the HT phases can be derived from the parent ABO_3 perovskite with the help of the structure modeling in the (3 + 1)-dimensional superspace.[19] The sequences of the ABO_2 and O_2 layers along the c direction for different n values can be obtained from a corresponding commensurate approximant of the modulated $A_nB_nO_{3n-2}$ structure with an orthorhombic $a = a_p\sqrt{2}$, $b = a_p$, $c = a_p\sqrt{2}$ average unit cell, $\mathbf{q} = \gamma\mathbf{c}^*$ ($\gamma = 1/n$) modulation vector, $Xmmm(00\gamma)000$ superspace group (X stands for the [1/2, 0, 1/2, 0]; [0, 1/2, 1/2, 1/2]; [1/2, 1/2, 0, 1/2] centering vectors), and the parameters of the step-like occupational modulation functions for the A, B, and O atoms given in Table S9, Supporting Information. Without taking into account atomic displacements, the space groups *Ammm* and *Imma* can be deduced from the superspace model for the homologues with n = odd and n = even, respectively. These are, indeed, the symmetries experimentally observed for the HT $A_nB_nO_{3n-2}$ structures.

Symmetry lowering upon transition to the LT phase occurs by freezing either the L or the R configuration of the tetragonal pyramidal chains. The refined LT $Pb_2Ba_2BiFe_5O_{13}$ and $Pb_{1.5}Ba_{2.5}Bi_2Fe_6O_{16}$ structures clearly show that the chains of the same configuration are arranged in layers, which are confined to the $1/2[110]_p(\bar{1}01)_p$ CS planes. This ordering can be associated with one of the irreducible representations of the space group of the HT phase. The irreducible representation generates the corresponding isotropy subgroup that describes the symmetry of the LT phase.[15,20] Such symmetry analysis is shown in Figure 10 for the $A_nB_nO_{3n-2}$ homologues with n = odd and n = even. In each case, two structures are possible: one with all CS planes having the same chain configuration, and the other one with alternating CS planes of the chains of different configurations.

At first glance, the switching between the R and the L configuration occurs due to a small lateral displacement of the oxygen atom O4 bridging the FeO_5 pyramids. This displacement does not require significant changes in interatomic

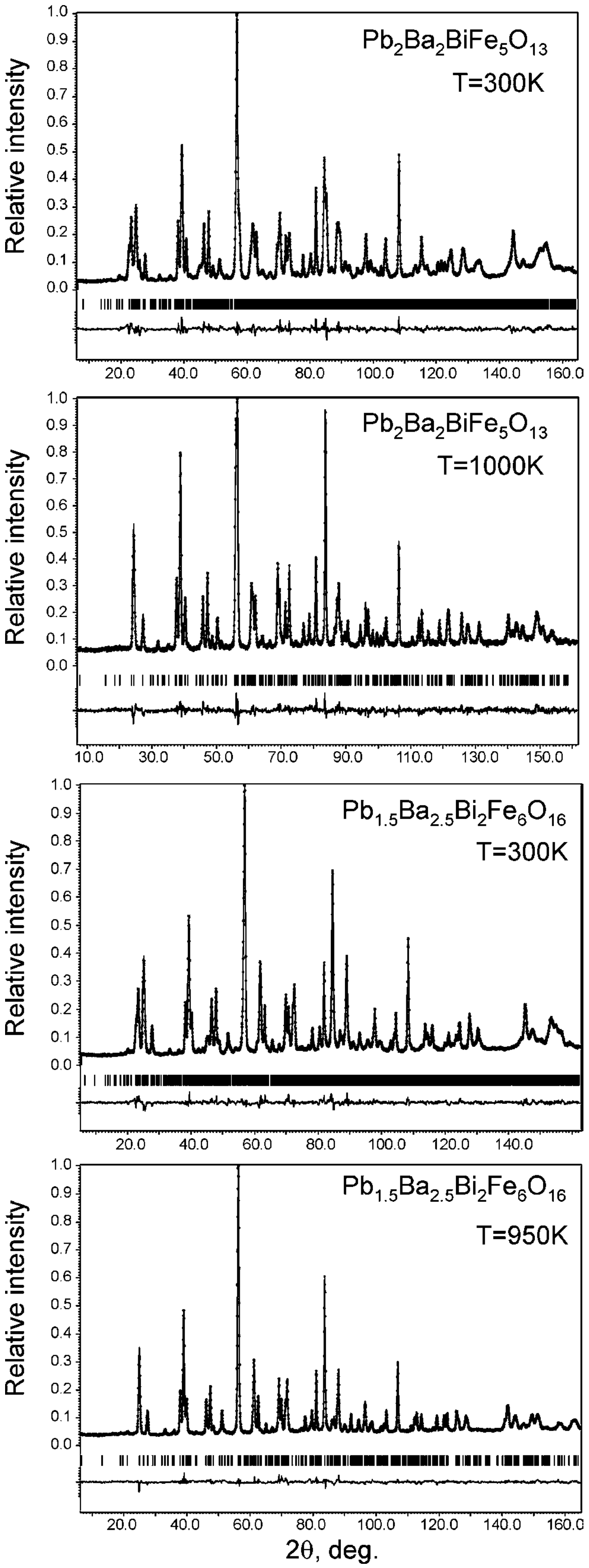

Figure 4. Experimental, calculated, and difference NPD profiles after Rietveld refinement of the LT and HT $Pb_2Ba_2BiFe_5O_{13}$ and $Pb_{1.5}Ba_{2.5}Bi_2Fe_6O_{16}$ structures.

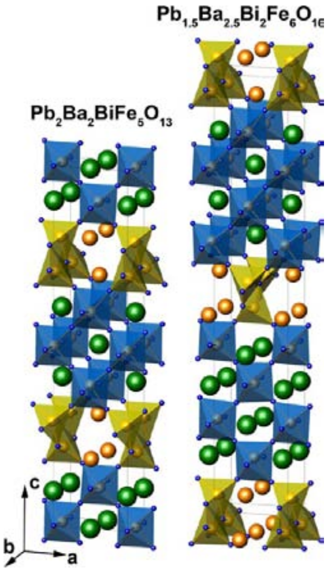

Figure 5. LT crystal structures of $Pb_2Ba_2BiFe_5O_{13}$ and $Pb_{1.5}Ba_{2.5}Bi_2Fe_6O_{16}$. FeO_6 octahedra are blue; FeO_5 tetragonal pyramids are yellow. A cations in the perovskite blocks and six-sided tunnels are shown as green and yellow spheres, respectively. Oxygen atoms are shown as small blue spheres.

distances and coordination spheres. One can expect that only a small free energy is associated with the chain ordering, and structures with different types of chain ordering have a similar probability of formation. However, the n = odd homologues demonstrate a preference toward a structure with equal chains ($Pb_2Ba_2BiFe_5O_{13}$), whereas for the n = even homologues the structure with alternating R and L chain layers is clearly preferable ($Pb_{2-x}A_xFe_2O_5$, A = Sr, Ba, $PbBaFeCoO_5$,[6,7,9,21] and $Pb_{1.5}Ba_{2.5}Bi_2Fe_6O_{16}$). The dependence of the chain order on the number of layers in the perovskite block reflects that the interaction between the chains can be mediated by the distortion of the perovskite blocks sandwiched between the CS planes. For example, chain ordering can be coupled to the cooperative octahedral tilting distortion.

The octahedral tilts are prohibited by symmetry in the HT phases, but in the LT phases the in-phase tilting component around the b axis ($a^0b^+a^0$ in the Glazer's notation) is allowed. In the homologues with n = odd, the perovskite blocks are delimited from both sides by the octahedra tilted in opposite directions, whereas tilts of the same sign occur for octahedra at the borders of the perovskite blocks in the n = even homologues. This can be intuitively linked with the fact that the LT phases with n = even adopt structures with chains of identical configuration, whereas in the n = odd LT phases CS planes with different chain configurations alternate. Indeed, a substantial octahedral tilt of ∼4° is observed in the Sr-based n = 4 phase.[6] However, in the Ba-based n = 4, 5, 6 homologues the octahedral tilt is strongly suppressed due to the larger ionic radius of the Ba^{2+} cation. Nevertheless, ordering of the chains also occurs in these compounds.

Although the octahedral tilt may play a certain role in arranging the chains of the pyramids, other effects leading to long-range interactions between the chains should be relevant as well. For instance, in brownmillerite-type ferrites, such as $Sr_2Fe_2O_5$, tetrahedral chains of two different configurations are present and also form a variety of ordered patterns.[22] Displacements of atoms from their ideal perovskite positions

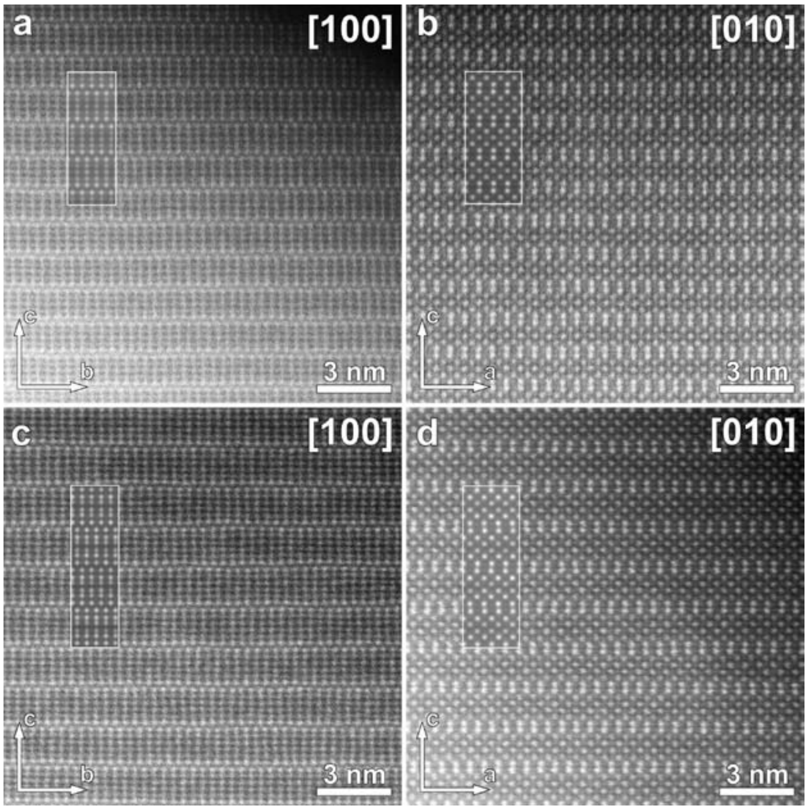

Figure 6. HAADF-STEM images for $Pb_2Ba_2BiFe_5O_{13}$ (a and b) and $Pb_{1.5}Ba_{2.5}Bi_2Fe_6O_{16}$ (c and d). Calculated images are shown as inserts. Simulations are made for the following crystal thicknesses: (a) 65, (b) 9, (c) 56, and (d) 81 Å.

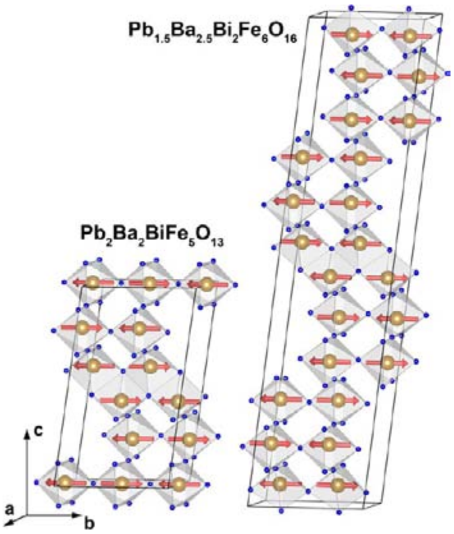

Figure 7. Magnetic structure of $Pb_2Ba_2BiFe_5O_{13}$ and $Pb_{1.5}Ba_{2.5}Bi_2Fe_6O_{16}$. Fe and O atoms are shown as brown and blue spheres, respectively. Pb, Ba, and Bi atoms are not shown for clarity. Magnetic unit cell is outlined. Unit cell axes of the nuclear structure are shown.

induce net dipole moments of the chains. Interaction between oppositely oriented dipoles of chains with different configurations is responsible for the chain order.[23−27] However, a larger data set on the structures of the LT $A_nB_nO_{3n-2}$ homologues would be needed to draw unambiguous conclusions and elaborate on the microscopic mechanism of the chain ordering.

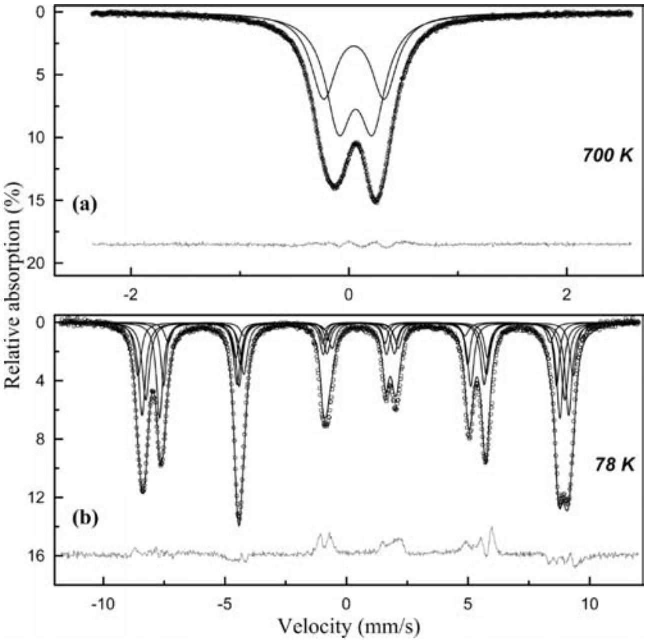

Figure 8. Mössbauer spectra of $Pb_2Ba_2BiFe_5O_{13}$ at $T = 700$ (a) and 78 K (b).

The HT → LT phase transition unavoidably results in a fragmentation of the structure into domains, related to each other by the symmetry elements that are lost below the transition temperature.[28,29] In the *Ammm* → *A*2/*m* transition observed in the n = odd materials, the translational symmetry remains intact but the lost mirror planes (the point group

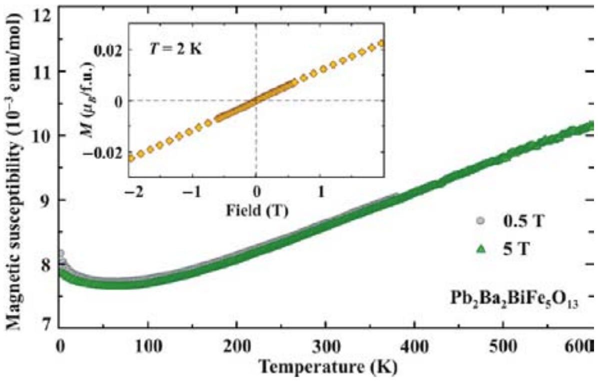

Figure 9. Magnetic susceptibility of $Pb_2Ba_2BiFe_5O_{13}$. (Inset) Magnetization curve measured at 2 K.

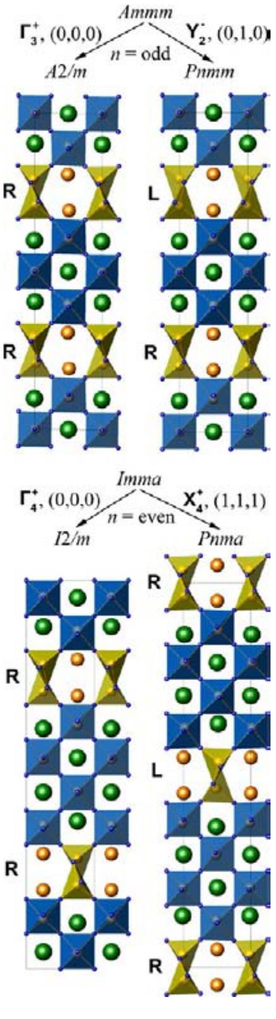

Figure 10. Symmetry lowering due to ordering of the R and L chains in the $A_nB_nO_{3n-2}$ structures with n = odd and n = even. Corresponding irreducible representation and superstructure wavevector are given for each case.

changes from *mmm* to 2/*m*) give rise to twin domains with the (001) plane as the twin plane, as can be seen from the reflection splitting on the [010] ED pattern (Figure 2). In contrast, the point group of the n = even compounds does not change upon *Imma* → *Pnma* phase transition, but the 1/2[111] body-centering translation is lost. Loss of the translational symmetry causes formation of antiphase boundaries (APBs). The APBs separate the domains of the LT *Pnma* structure that are shifted with respect to each other by the translation vector lost in the transition, i.e., 1/2[111]. Closely separated APBs parallel to the (001) plane cause the diffuse intensity lines parallel to **c***, as observed experimentally (Figure 3 and Figure S2, Supporting Information). At high concentration, APBs may coalesce and form domains of the monoclinic *I*2/*m* phase in the *Pnma* matrix. This type of defect underlies the broadening of the *h*0*l* reflections on the SXPD pattern of $Pb_{1.5}Ba_{2.5}Bi_2Fe_6O_{16}$. Since the concentration of APBs is temperature dependent, broadening varies with temperature as well.

All n = 4, 5, and 6 members of the $A_nFe_nO_{3n-2}$ (A = Pb, Bi, Ba) ferrites demonstrate similar antiferromagnetic transition temperatures: T_N = 625 K for $Pb_{1.08}Ba_{0.92}Fe_2O_5$,[9] T_N = 623 K for $Pb_2Ba_2BiFe_5O_{13}$, and T_N = 632 K for $Pb_{1.5}Ba_{2.5}Bi_2Fe_6O_{16}$. The Néel temperature is nearly independent of the thickness of the perovskite blocks and of the chemical composition. This observation indirectly confirms that despite changes in the cation composition the anion deficiency is fully accommodated by the CS planes, thus resulting in a constant oxidation state of +3 for the Fe atoms. The observed AFM structure of the n = 5 and 6 materials agrees well with the nature of the main exchange couplings obtained for the n = 4 $PbBaFe_2O_5$ compound using density-functional band structure calculations.[1] The G-type AFM ordering within the perovskite blocks is governed by the dominating ~180° Fe−O−Fe AFM exchange, including interaction J_2 between the edge-sharing pyramids (Figure 11). The interaction between the blocks corresponds to ~10 times weaker ~90 °FM coupling J_1 (Figure 11). This interblock coupling is apparently frustrated, since the AFM alignment of spins imposed by J_2 does not allow all J_1 to be satisfied simultaneously. Nevertheless, despite weak and frustrated interblock exchange couplings, all $A_nFe_nO_{3n-2}$ ferrites feature robust AFM ordering with relatively high Néel temperatures. The magnetic order between the blocks can be tentatively ascribed to dipolar interactions that are responsible for interlayer ordering in other layered perovskites, such as Rb_2MnF_4.[30]

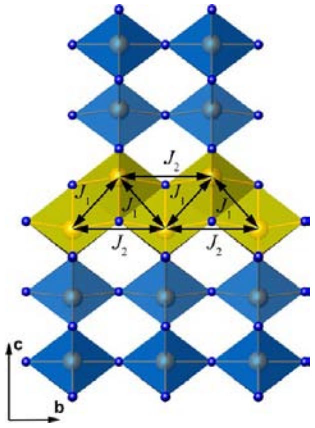

Figure 11. Main exchange couplings in the $A_nB_nO_{3n-2}$ structures: ~90° Fe−O−Fe FM J_1 exchange and ~180° Fe−O−Fe AFM J_2 exchange.

■ ASSOCIATED CONTENT

Ⓢ Supporting Information

Compositional dependence of the lattice parameters for the $Pb_{2-x}Ba_{2+x}Bi_2Fe_6O_{16}$ solid solutions, temperature-dependent

SXPD patterns, temperature-dependent ED patterns of $Pb_{1.5}Ba_{2.5}Bi_2Fe_6O_{16}$, temperature dependence of the lattice parameters and unit cell volume for $Pb_2Ba_2BiFe_5O_{13}$ and $Pb_{1.5}Ba_{2.5}Bi_2Fe_6O_{16}$, HAADF-STEM image of stacking faults in the $Pb_2Ba_2BiFe_5O_{13}$, parameters of the magnetic structures, temperature dependence of the magnetic moments for $Pb_2Ba_2BiFe_5O_{13}$ and $Pb_{1.5}Ba_{2.5}Bi_2Fe_6O_{16}$, Mössbauer parameters for $Pb_2Ba_2BiFe_5O_{13}$, parameters of the superspace model for $A_nB_nO_{3n-2}$ structures, magnetic susceptibility measurements for $Pb_{1.5}Ba_{2.5}Bi_2Fe_6O_{16}$. This material is available free of charge via the Internet at http://pubs.acs.org.

■ AUTHOR INFORMATION

Corresponding Author

*E-mail: artem.abakumov@ua.ac.be.

Notes

The authors declare no competing financial interest.

■ ACKNOWLEDGMENTS

We acknowledge the funding from the Research Foundation—Flanders under grant no. G.0184.09N and Russian Foundation of Basic Research under grant no. 11-03-01257a. G.V.T. acknowledges financial support from ERC grant no. 246791-COUNTATOMS. A.T. was supported by the Mobilitas grant of the ESF. We are grateful to the Paul Scherrer Institute (Switzerland) and ESRF for granting the beam time at HRPT and ID31, respectively. Experimental support of Andy Fitch (ESRF) is kindly acknowledged.

■ REFERENCES

(1) Abakumov, A. M.; Hadermann, J.; Batuk, M.; D'Hondt, H.; Tyablikov, O. A.; Rozova, M. G.; Pokholok, K. V.; Filimonov, D. S.; Sheptyakov, D. V.; Tsirlin, A. A.; Niermann, D.; Hemberger, J.; Van Tendeloo, G.; Antipov, E. V. *Inorg. Chem.* **2010**, *49*, 9508−9516.

(2) Abakumov, A. M.; Hadermann, J.; Bals, S.; Nikolaev, I. V; Antipov, E. V; Van Tendeloo, G. *Angew. Chem.* **2006**, *45*, 6697−700.

(3) Abakumov, A. M.; Hadermann, J.; Van Tendeloo, G.; Antipov, E. V. *J. Am. Ceram. Soc.* **2008**, *91*, 1807−1813.

(4) Anderson, M. T.; Vaughey, J. T.; Poeppelmeier, K. R. *Chem. Mater.* **1993**, *5*, 151−165.

(5) Hadermann, J.; Van Tendeloo, G.; Abakumov, A. M. *Acta Crystallogr., Sect. A* **2005**, *61*, 77−92.

(6) Raynova-Schwarten, V.; Massa, W.; Babel, D. *Z. Anorg. Allg. Chem.* **1997**, *623*, 1048−1054.

(7) Tzvetkov, P.; Petrova, N.; Kovacheva, D. *J. Alloys Compd.* **2009**, *485*, 862−866.

(8) Hadermann, J.; Abakumov, A. M.; Perkisas, T.; D'Hondt, H.; Tan, H.; Verbeeck, J.; Filonenko, V. P.; Antipov, E. V.; Van Tendeloo, G. *J. Solid State Chem.* **2010**, *183*, 2190−2195.

(9) Nikolaev, I.; D'Hondt, H.; Abakumov, A. M.; Hadermann, J.; Balagurov, A.; Bobrikov, I.; Sheptyakov, D.; Pomjakushin, V.; Pokholok, K.; Filimonov, D.; Van Tendeloo, G.; Antipov, E. *Phys. Rev. B* **2008**, *78*, 024426.

(10) Korneychik, O. E.; Batuk, M.; Abakumov, A. M.; Hadermann, J.; Rozova, M. G.; Sheptyakov, D. V.; Pokholok, K. V.; Filimonov, D. S.; Antipov, E. V. *J. Solid State Chem.* **2011**, *184*, 3150−3157.

(11) Petricek, V.; Dusek, M.; Palatinus, L. *The crystallographic computing system JANA2006*; Institute of Physics: Praha, Czech Republic. 2006.

(12) Koch, C. *Determination of core structure and periodicity and point defect density along dislocations*; Arizona State University: Phoenix, AZ, 2002.

(13) Watson, G. W.; Parker, S. C.; Kresse, G. *Phys. Rev. B* **1999**, *59*, 8481−8486.

(14) Watson, G. W.; Parker, S. C. *J. Phys. Chem. B* **1999**, *103*, 1258−1262.

(15) Campbell, B. J.; Stokes, H. T.; Tanner, D. E.; Hatch, D. M. *J. Appl. Crystallogr.* **2006**, *39*, 607−614.

(16) Menil, F. *J. Phys. Chem. Solids.* **1985**, *46*, 763−789.

(17) Néel, L. *Ann. Phys.—Paris* **1948**, *3*, 137.

(18) Smit, J.; Wijn, H. P. J. *Ferrites*; Phillips Technical Library, 1959.

(19) Perez-Mato, J. M.; Zakhour-Nakhl, M.; Weill, F.; Darriet, J. *J. Mater. Chem.* **1999**, *9*, 2795−2808.

(20) Howard, C. J.; Stokes, H. T. *Acta Crystallogr., Sect. B* **1998**, *54*, 782−789.

(21) Tzvetkov, P.; Kovacheva, D.; Nihtianova, D.; Ruskov, T. *Bulg. Chem. Comm.* **2011**, *43*, 339−345.

(22) D'Hondt, H.; Abakumov, A. M.; Hadermann, J.; Kalyuzhnaya, A. S.; Rozova, M. G.; Antipov, E. V.; Van Tendeloo, G. *Chem. Mater.* **2008**, *20*, 7188−7194.

(23) Krekels, T.; Milat, O.; Van Tendeloo, G.; Amelinckx, S.; Babu, T. G. N.; Wright, A. J.; Greaves, C. *J. Solid State Chem.* **1993**, *105*, 313−335.

(24) Abakumov, A. M.; Alekseeva, A. M.; Rozova, M. G.; Antipov, E. V.; Lebedev, O. I.; Van Tendeloo, G. *J. Solid State Chem.* **2003**, *174*, 319−328.

(25) Abakumov, A. M.; Kalyuzhnaya, A. S.; Rozova, M. G.; Antipov, E. V.; Hadermann, J.; Van Tendeloo, G. *Solid State Sci.* **2005**, *7*, 801−811.

(26) Hadermann, J.; Abakumov, A. M.; D'Hondt, H.; Kalyuzhnaya, A. S.; Rozova, M. G.; Markina, M. M.; Mikheev, M. G.; Tristan, N.; Klingeler, R.; Büchner, B.; Antipov, E. V. *J. Mater. Chem.* **2007**, *17*, 692−698.

(27) Parsons, T. G.; D'Hondt, H.; Hadermann, J.; Hayward, M. A. *Chem. Mater.* **2009**, *21*, 5527−5538.

(28) Van Tendeloo, G.; Amelinckx, S. *Acta Crystallogr., Sect. A* **1974**, *30*, 431−440.

(29) Boulesteix, C.; Van Landuyt, J.; Amelinckx, S. *Phys. Status Solidi A* **1976**, *33*, 595−606.

(30) Zhou, C.; Landau, D. P.; Schulthess, T. C. *Phys. Rev. B* **2007**, *76*, 024433.